



Si-core photonic crystal fiber transverse-electric pass polarizer

JIDEFOR A. H. ODOEZE,^{1,2,3}  MOHAMED FARHAT O. HAMEED,^{3,4,5}  HOSSAM M. H. SHALABY,² 
AND SALAH S. A. OBAYYA^{3,5,*} 

¹Department of Electronic Engineering, Faculty of Engineering, University of Nigeria, Nsukka 410001, Nigeria

²Department of Electronics and Communications Engineering, Egypt-Japan University of Science and Technology (E-JUST), Alexandria 21934, Egypt

³Center for Photonics and Smart Materials, Zewail City of Science and Technology, October Gardens, 6th of October City, Giza, Egypt

⁴Nanotechnology Engineering Program, University of Science and Technology, Zewail City of Science and Technology, 6th of October, October Gardens, Giza, Egypt

⁵Faculty of Engineering, Mansoura University, Egypt, Mansoura 35516, Egypt

*Corresponding author: sobayya@zewailcity.edu.eg

Received 18 January 2018; revised 27 February 2018; accepted 27 February 2018; posted 28 February 2018 (Doc. ID 319969); published 4 April 2018

Photonic crystal fibers (PCFs) have been extensively used in literature for designing polarization handling devices. Further, the Si material has advantages in terms of low loss transmission with a high refractive index. In this paper, a novel design of transverse-electric (TE) pass polarizer based on Si-core photonic crystal fiber (SC-PCF) is reported and studied using full vectorial finite element method. The suggested PCF has a SiO₂ cladding background and is selectively filled with gold nanorods. Further, an elliptical Si-core is used to increase the birefringence between the two polarizing modes. Therefore, the surface plasmon modes around the gold nanorods are highly coupled with the quasi-transverse-magnetic (TM) core modes while no coupling occurs with the quasi-TE core mode. Consequently, high and low confinement losses are achieved for the quasi-TM and quasi-TE core modes, respectively. Accordingly, a TE-pass polarizer is realized with an insertion loss of -0.000108 dB. Additionally, a good extinction ratio of -13.18 dB is obtained at a short device length of $29 \mu\text{m}$. © 2018 Optical Society of America

OCIS codes: (230.7370) Waveguides; (240.6680) Surface plasmons; (130.5296) Photonic crystal waveguides; (250.5403) Plasmonics.

<https://doi.org/10.1364/JOSAB.35.000980>

1. INTRODUCTION

The capacity of systems has been increased by the use of multiplexing techniques [1,2]. Mode-division multiplexing (MDM) has been shown to be more suitable for photonic integrated circuits (PIC) [3,4]. However, power transfer between the two orthogonal modes may occur in MDM systems, which is a major problem in communications and sensing systems [5]. Accordingly, there is a serious need for polarization handling devices, which include polarization beam splitters, polarization rotators, and polarizers. The conventional polarizer is based on bulk birefringent crystals. Therefore, it is mandatory to design compact polarizers that can be integrated on PIC. This gave rise to silicon-on-insulator (SOI) polarizers [6]. SOI devices have advantages in terms of low cost and high compatibility with CMOS as well as silicon sources and detectors [7]. Many SOI-based transverse electric (TE)/transverse magnetic (TM)-pass polarizers are available in literature. Dai *et al.*

have proposed a TE-pass polarizer with a device length of 1 mm [6]. Alam *et al.* have introduced a compact hybrid TM-pass polarizer for SOI platforms [8]. Hyuang *et al.* demonstrated a CMOS-compatible SOI horizontal nanoplasmonic slot waveguides TE-pass polarizer [9]. Sun *et al.* have reported experimentally compact hybrid TE-pass polarizer [10] with an insertion loss (IL) less than 0.04 dB [11]. Furthermore, Azzam *et al.* investigated compact SOI-based TE/TM-pass polarizers based on resonant tunneling process [12]. Additionally, CMOS-compatible TE/TM-pass polarizers based on titanium nitride have been reported with an IL of 0.0635 dB [13]. Recently, Hameed *et al.* have proposed an ultrashort hybrid plasmonic TE-pass polarizer for SOI platforms with IL of 0.1639 dB [14]. The exceptional electronic transport properties of graphene [15] alongside its equally remarkable photonic properties [16] have enabled graphene-based polarizers. Qiaoliang *et al.* have demonstrated a broadband fiber polarizer

based on graphene, an ultrathin two-dimensional carbon material [17]. Additionally, Xiang *et al.* proposed and demonstrated a novel silicon slot waveguide ultra-compact TE-pass polarizer with graphene multilayer embedded in the slot [18]. Further, Xiang *et al.* have proposed and demonstrated an ultra-broadband TE-pass polarizer using a cascade of multiple few-layer graphene embedded silicon waveguides [19]. Tian *et al.* have also utilized a graphene-based asymmetrical directional coupler to achieve an ultra-compact polarization beam splitter [20]. Furthermore, Ghosh *et al.* have reported graphene oxide integrated on-chip tunable waveguide polarizer [21]. Photonic crystal fibers (PCFs) are periodic micro-structures that are known for their low loss [22,23], endlessly single-mode guidance, and dispersion control. The light wave is guided through either solid core or hollow core using total internal reflection or photonic bandgap guidance, respectively [24]. Many PCF polarizers are available in the literature. Lee *et al.* reported polarization-dependent coupling to plasmon modes on sub-micron gold wire in PCF [25]. Additionally, Heikal *et al.* presented an efficient polarization filter based on plasmonic PCF [26]. Further, Hameed *et al.* reported an ultra-high tunable liquid crystal-plasmonic PCF polarization filter with loss of 0.00751 dB/cm and 0.092 dB/cm for the x -polarized mode and y -polarized mode, respectively [24]. Recently, Li *et al.* have reported a dual-wavelength single polarizing filter based on PCF [27]. Silicon (Si) material has a high refractive index, which enhances light confinement through a small area. Further, silicon has high material reliability and stability with CMOS technology [28]. Such good characteristics of silicon have been integrated with optical fibers to produce low-loss silicon fibers [29] and hollow-core PCF [30]. Silicon fibers can be fabricated using high-pressure microfluidic chemical deposition techniques, which deposit silicon into silica capillaries [31]. Therefore, the combination between silicon and PCF has a great potential for obtaining low-loss polarization handling devices.

In this paper, a compact design of PCF TE-pass polarizer is reported and studied. The suggested PCF has a background material of SiO_2 and solid core of Si. The silicon solid core has an elliptical shape to increase the birefringence between the two fundamental core guided modes [32,33]. Gold nanorods are selectively injected into the cladding holes to control the confinement losses of the two polarized modes. Due to the elliptical shape of the silicon core, strong coupling occurs between the surface plasmon (SP) modes with the quasi-TM mode. However, the quasi-TE mode has no coupling with low losses. Therefore, a TE-pass polarizer of compact length of 29 μm is achieved with a very low IL of -0.000108 dB and good extinction ratio of -13.18 dB. Simulation results are calculated via COMSOL Multiphysics software [34] based on the full vectorial finite element method. Furthermore, time domain simulation is performed using finite-difference time-domain (FDTD) method based on Lumerical software package [35] to ensure the filtering characteristics of the proposed polarizer.

2. DESIGN CONSIDERATIONS

The cross sections of the proposed PCF polarizer with different numbers N of gold nanorods are shown in Fig. 1.

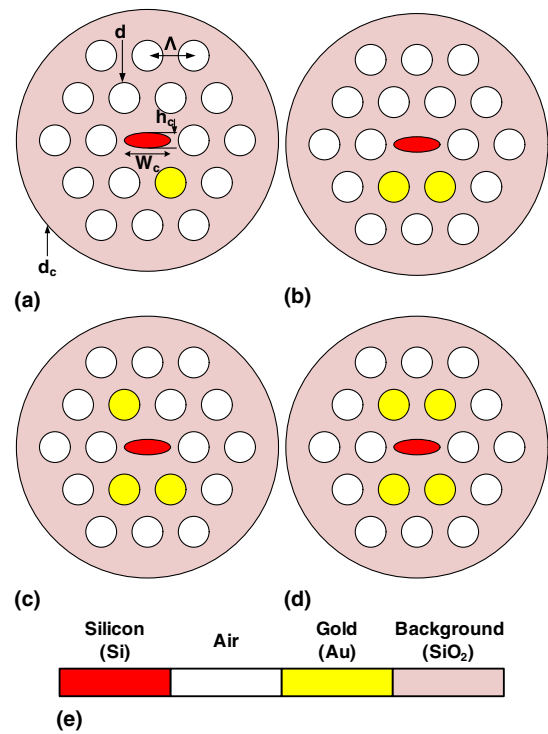


Fig. 1. Proposed Si-core PCF selectively infiltrated by gold nanorods with N rods, where (a) $N = 1$, (b) $N = 2$, (c) $N = 3$, (d) $N = 4$. (e) Color code.

The suggested SC-PCF has SiO_2 as a background material with diameter $d_c = 2.11 \mu\text{m}$ and an elliptical Si core with a major axis diameter $W_c = 0.6 \mu\text{m}$ and a minor axis diameter $h_c = 0.22 \mu\text{m}$. The core is surrounded by two successive rings of air holes of diameter d . The air holes are arranged in a periodic triangular lattice with a hole pitch of $\Lambda = 0.74 \mu\text{m}$. The cladding air holes are selectively infiltrated with gold nanorods as shown in Fig. 1. The relative permittivity of gold nanoparticles is calculated using the Drude model given in [14,24,26]

$$\epsilon_{\text{Au}}(\omega) = \epsilon_{\infty} - \frac{\omega_p^2}{\omega(\omega + \Im\omega_{\tau})}, \quad (1)$$

where ω is the angular frequency, $\epsilon_{\infty} = 9.75$ is the high-frequency dielectric constant, $\omega_p = 1.36 \times 10^{16}$ rad/s is the plasma frequency, and $\omega_{\tau} = 1.45 \times 10^{14}$ rad/s is the damping frequency. The relative permittivity of SiO_2 is calculated using the Sellmeier equation as given in [26,36]

$$n_{\text{SiO}_2}^2(\lambda) = 1 + \frac{A_1\lambda^2}{\lambda^2 - \lambda_1^2} + \frac{A_2\lambda^2}{\lambda^2 - \lambda_2^2} + \frac{A_3\lambda^2}{\lambda^2 - \lambda_3^2}, \quad (2)$$

where $n_{\text{SiO}_2}(\lambda)$ represents the wavelength-dependent refractive index of silica, $A_1 = 0.6961663$, $A_2 = 0.4079426$, $A_3 = 0.8974794$, $\lambda_1 = 0.0684043 \mu\text{m}$, $\lambda_2 = 0.1162414 \mu\text{m}$, and $\lambda_3 = 9.896161 \mu\text{m}$. Similarly, the relative permittivity of Si is calculated at room temperature (298 K) from the following Sellmeier equation [37]:

$$n_{\text{Si}}^2(\lambda) = \epsilon + \frac{A}{\lambda^2} + \frac{A_2\nu^2}{\lambda^2 - \nu^2}, \quad (3)$$

where $n_{\text{Si}}(\lambda)$ is the wavelength-dependent refractive index of silicon, $\varepsilon = 11.6858$, $A = 0.939816 \mu\text{m}$, $A_2 = 8.10461 \times 10^{-3}$, and $\nu = 1.1071 \mu\text{m}$.

3. SIMULATION RESULTS

In this investigation, full vectorial finite element method (FVFEM) based on COMSOL 5.1 Multiphysics software package [34] is used to study and analyze the reported PCF. A circular computational domain of diameter $d_c = 2.11 \mu\text{m}$, with 46,366 degrees of freedom, and minimum element size of $9.66 \times 10^{-4} \mu\text{m}$ are used. The perfect matched layer (PML) is also used as absorbing boundary conditions. The full vectorial eigenvalue equation is given by

$$[K]\{H\} - \beta^2[M]\{H\} = \{0\}. \quad (4)$$

The FVFEM solves Eq. (4) to obtain the magnetic field eigenvector \mathbf{H} and the corresponding propagation constant eigenvalue β of the supported modes where the effective index $n_{\text{eff}} = \beta/k$, and k is the free-space wave number. The global stiffness and mass matrices are denoted by $[K]$ and $[M]$, respectively while $\{0\}$ is the null vector. The modal confinement loss (L) is calculated from the imaginary part of the effective index using the formula in [38],

$$L(\text{dB}/\mu\text{m}) = \frac{20}{\ln(10)} \cdot \frac{2\pi}{\lambda} \cdot \Im(n_{\text{eff}}), \quad (5)$$

where λ is wavelength in micrometers (μm). The insertion losses (ILs) and extinction ratios (ERs) of the propagating modes through the device are calculated using 3D finite-difference time-domain (3D-FDTD) from Lumerical software [35],

$$\text{IL}(\text{dB}) = 10 \log_{10} \left(\frac{P_{\text{out}}^{\text{TE}}}{P_{\text{in}}^{\text{TE}}} \right) \quad (6)$$

and

$$\text{ER}(\text{dB}) = 10 \log_{10} \left(\frac{P_{\text{out}}^{\text{TE}}}{P_{\text{in}}^{\text{TE}}} \times \frac{P_{\text{out}}^{\text{TM}}}{P_{\text{in}}^{\text{TM}}} \right), \quad (7)$$

where $(P_{\text{out}}^{\text{TE}}$ and $P_{\text{in}}^{\text{TE}})$ and $(P_{\text{out}}^{\text{TM}}$ and $P_{\text{in}}^{\text{TM}})$ are the output and input powers of the quasi-TE and quasi-TM core modes, respectively. It is aimed to design a compact TE-pass polarizer based on the reported structure with low insertion losses and good extinction ratio. Therefore, the geometrical parameters of the Si-core PCF are studied to get the best performance of the proposed TE-pass polarizer. Initially, we set $W_c = 0.6 \mu\text{m}$, $h_c = 0.22 \mu\text{m}$, and $d = 0.1 \mu\text{m}$ with operating wavelength of $\lambda = 1.55 \mu\text{m}$. The modal characteristics of the two orthogonal polarization states of the fundamental core modes are first calculated, taking into account the number of gold nanorods N and the hole pitch Λ . Figure 2 shows the variations of the n_{eff} and confinement losses of the two polarized modes with the hole pitch at different numbers of gold nanorods. It is seen from Fig. 2(a) that there is high birefringence between the effective indices of the quasi-TE and quasi-TM fundamental core modes due to the elliptical core region. Further, the quasi-TE core mode has a greater effective index than the quasi-TM core mode for all studied cases as shown in Fig. 2(a). This is due to better confinement of the quasi-TE core mode in the high-index Si-core region. In the same Fig. 2(a), the quasi-TE mode n_{eff} is seemingly unaffected

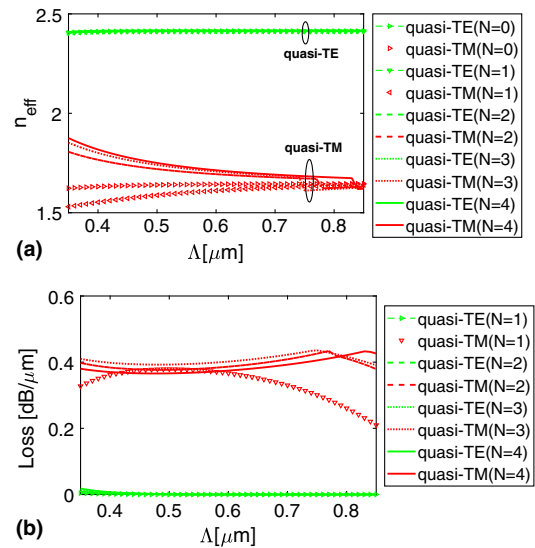


Fig. 2. Effect of hole pitch and number of rods (N) on the modal characteristics of the two polarized core modes at $\lambda = 1.55 \mu\text{m}$, $W_c = 0.6 \mu\text{m}$, $h_c = 0.22 \mu\text{m}$, and $d = 0.1 \mu\text{m}$ on the (a) effective index n_{eff} , and (b) confinement loss in $\text{dB}/\mu\text{m}$.

by the variations in the hole pitch and the number of gold nanorods, whereas the quasi-TM core mode n_{eff} is affected significantly. Figure 2(b) shows that the confinement losses of the quasi-TE core mode are far smaller (almost negligible) than that of the quasi-TM core mode. It is also seen from Fig. 2(b) that at a hole pitch of $\Lambda = 0.74 \mu\text{m}$ and $N = 3$, the quasi-TM core mode has a maximum loss. Figure 3 shows the field plots (H_y and H_x) of the quasi-TE core mode, quasi-TM core mode, SP_{TM} mode, and SP_{TE} mode at $\lambda = 1.55 \mu\text{m}$. It is evident from Fig. 3(a) that there is very low or no coupling between the SP mode and the quasi-TE core mode. However, the quasi-TM core mode has large losses due to the strong coupling between the SP mode around the gold nanorods and the quasi-TM core modes as shown in Fig. 3(f). Therefore, it is expected that a TE-pass polarizer can be designed based on the suggested PCF.

Next, the effects of the cladding hole diameters d , including the gold nanorods on the confinement loss of the two polarized modes, are discussed at $\Lambda = 0.74 \mu\text{m}$, $N = 3$, and $\lambda = 1.55 \mu\text{m}$. The variation of the confinement loss with the cladding hole diameter d is shown in Fig. 4, where a maximum loss is obtained at $d = 0.1 \mu\text{m}$. Figure 5 shows the variation of confinement loss and effective indices of the quasi-TE, quasi-TM, and SP modes with the wavelength. It is shown that at $\lambda = 1.55 \mu\text{m}$, the effective indices of the quasi-TM mode and the SP mode are almost equal, and hence coupling between them occurs. It is also evident from Fig. 5(b) that the loss of the quasi-TM mode increases rapidly between wavelength of 1.45 to $1.6 \mu\text{m}$, where the coupling with the SP modes starts to increase. At $\lambda = 1.55 \mu\text{m}$, the losses of the quasi-TM and quasi-TE modes are equal to $0.4343 \text{ dB}/\mu\text{m}$ and $1 \times 10^{-5} \text{ dB}/\mu\text{m}$, respectively.

The impact of the major and minor diameters of the elliptical Si core is also investigated. Figures 6 and 7 show the variation of the confinement losses and effective indices of

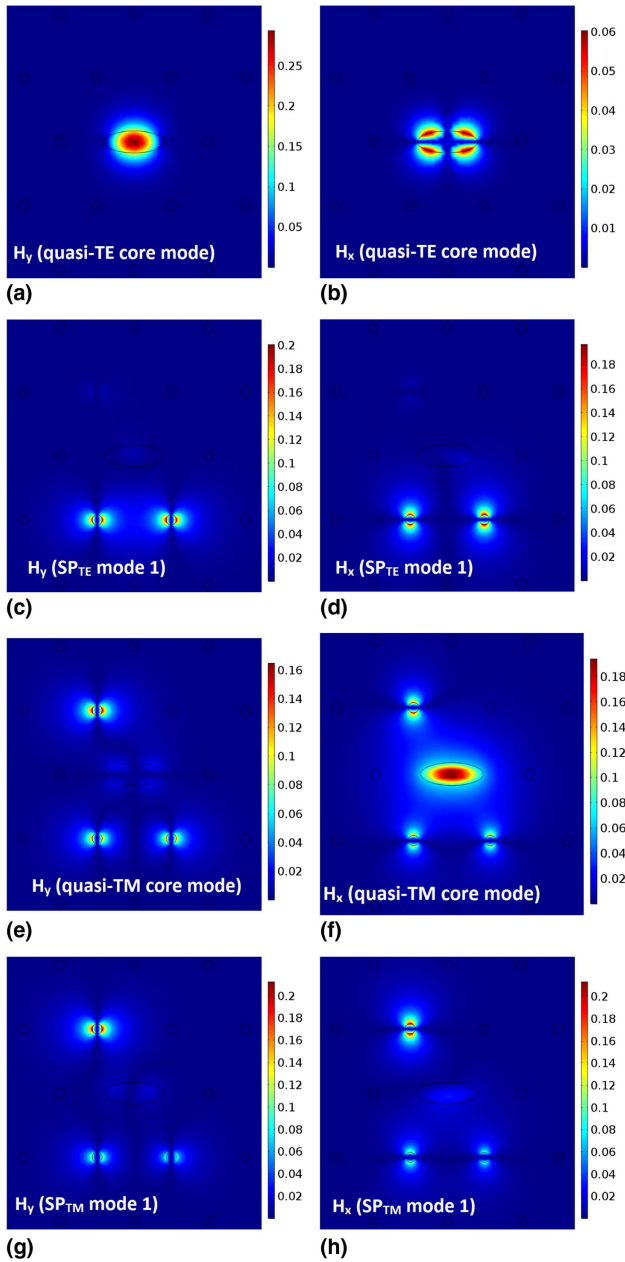


Fig. 3. Field plots of (a) H_y of quasi-TE core mode, (b) H_x of quasi-TE core mode, (c) H_y of SP_{TE} mode, (d) H_x of SP_{TE} mode, (e) H_y of quasi-TM core mode, (f) H_x of quasi-TM core mode, (g) H_y of SP_{TM} mode, and (h) H_x of SP_{TM} mode at $\lambda = 1.55 \mu\text{m}$, $W_c = 0.6 \mu\text{m}$, $h_c = 0.22 \mu\text{m}$, $d = 0.1 \mu\text{m}$, $N = 3$, and $\Lambda = 0.74 \mu\text{m}$.

the two polarized modes with W_c (at $h_c = 0.22 \mu\text{m}$) and h_c (at $W_c = 0.6 \mu\text{m}$), respectively. It is revealed from Figs. 6(a) and 7(a) that high birefringence is obtained due to the elliptical nature of the core. When W_c is equal to h_c , the birefringence is very low while the birefringence increases significantly by increasing the difference between the two axes of the elliptical core. The loss plot of Figs. 6(b) and 7(b) show that the quasi-TM fundamental core mode loss is maximum at $W_c = 0.6 \mu\text{m}$ and $h_c = 0.22 \mu\text{m}$, respectively. Additionally, there will be no significant birefringence if a circular core is used.

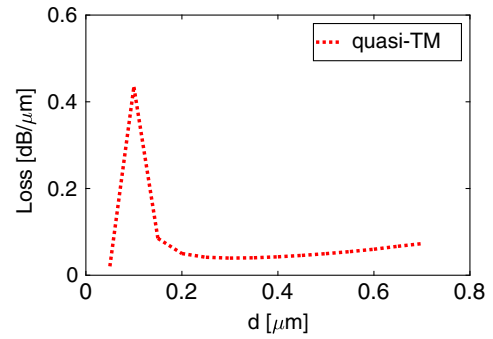


Fig. 4. Effect of the cladding air hole and gold nanorod diameters d on the confinement loss of the quasi-TM mode.

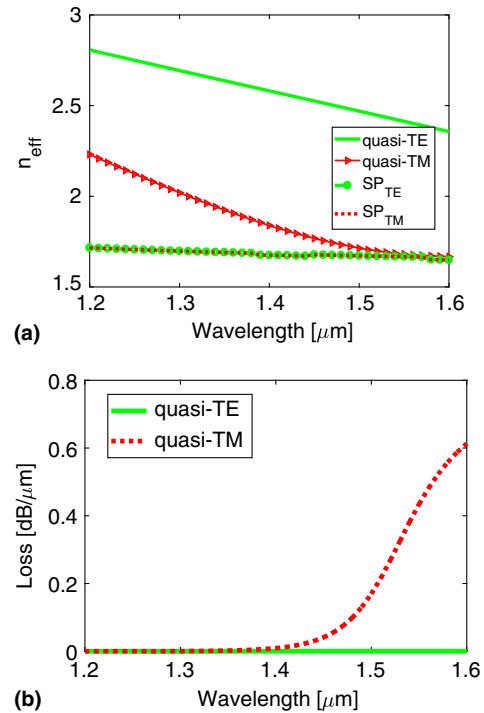


Fig. 5. Effect of the wavelength on the (a) n_{eff} , and (b) loss of the two polarized modes core modes at $W_c = 0.6 \mu\text{m}$, $h_c = 0.22 \mu\text{m}$, $d = 0.1 \mu\text{m}$, $N = 3$, and $\Lambda = 0.74 \mu\text{m}$. The n_{eff} of the SP_{TE} and SP_{TM} are also shown in Fig. 5(a).

Therefore, an elliptical solid core is mandatory to facilitate the filtering process of one polarized mode.

To test the filtering characteristics of the reported TE-pass polarizer, the propagation of the quasi-TE and quasi-TM core mode through the device is studied using Lumerical 3D finite-difference time-domain (3D-FDTD) software. In order to calculate the IL and ER, expansion mode monitor was used to accurately measure the power of a particular mode. Figure 8 shows the variation of IL and ER with the device length L . At $\lambda = 1.55 \mu\text{m}$, $N = 3$, $d = 0.1 \mu\text{m}$, $\Lambda = 0.74 \mu\text{m}$, and $L = 29 \mu\text{m}$, a very low IL of -0.000108 dB and good ER of -13.18 dB are reported. Further, a monitor is placed on top of the device to calculate the electric field powers of the

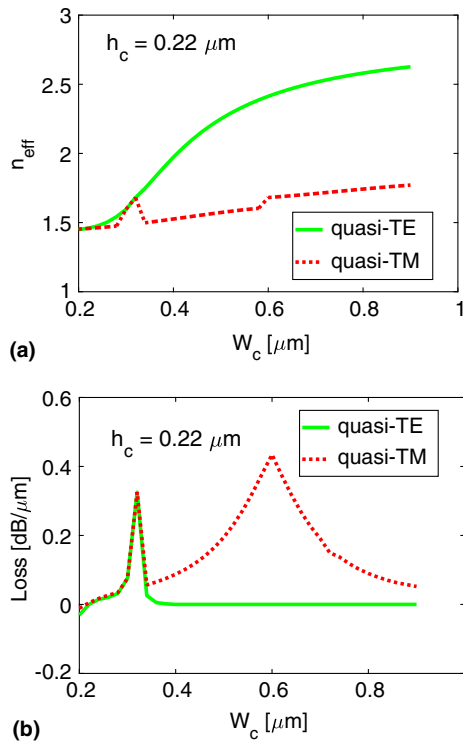


Fig. 6. Effect of W_c on the (a) n_{eff} , and (b) loss of the two polarized core modes at $\lambda = 1.55 \mu\text{m}$, $h_c = 0.22 \mu\text{m}$, $d = 0.1 \mu\text{m}$, $N = 3$, and $\Lambda = 0.74 \mu\text{m}$.

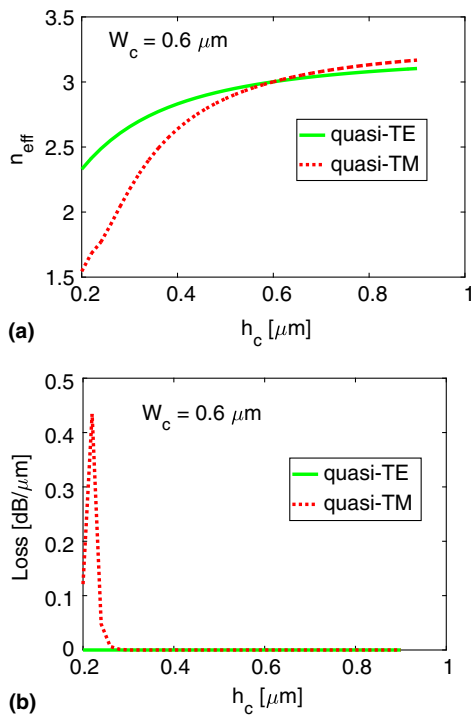


Fig. 7. Effect of h_c on the (a) n_{eff} , and (b) loss of the two polarized core modes at $\lambda = 1.55 \mu\text{m}$, $W_c = 0.6 \mu\text{m}$, $d = 0.1 \mu\text{m}$, $N = 3$, and $\Lambda = 0.74 \mu\text{m}$.

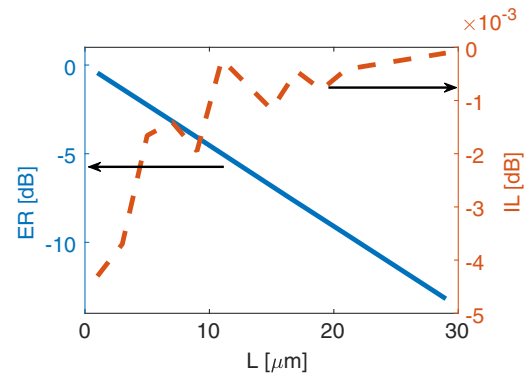


Fig. 8. Variation of the IL and ER with the device length (L).

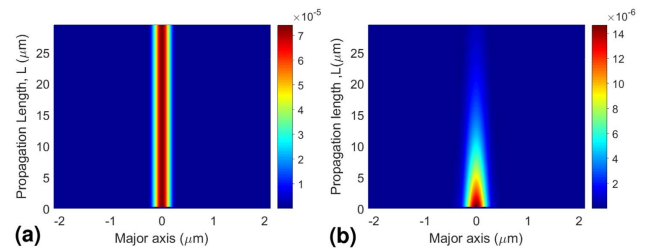


Fig. 9. Light propagation through the suggested TE-pass polarizer of the (a) quasi-TE mode and (b) quasi-TM mode.

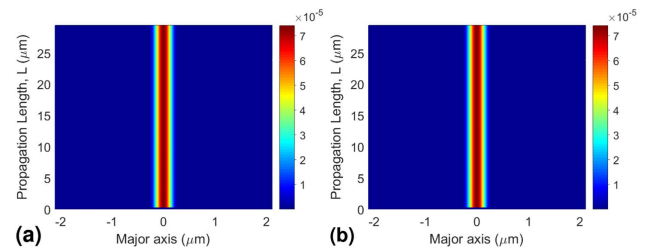


Fig. 10. Light propagation through the suggested TE-pass polarizer without gold nanorods of the (a) quasi-TE mode and (b) quasi-TM mode.

quasi-TE mode and quasi-TM core mode during the propagation as shown in Fig. 9. It is evident from Fig. 9(a) that quasi-TE core mode passes through the suggested design with negligible loss, whereas the quasi-TM core mode is attenuated greatly. Hence, a TE-pass polarizer is achieved. It is important to note that if the gold nanorods are removed, we would have the electric field propagation through the device as shown in Fig. 10. The quasi-TE and quasi-TM core modes propagation as seen in Figs. 10(a) and 10(b), respectively, show that there is no attenuation of any mode that ensures that the filtering is due to the gold nanorods. In order to show the efficiency of the suggested polarizer, the wavelength dependency of the insertion losses and crosstalk are calculated as shown in Fig. 11. It may be seen from this figure that the reported design has a very low insertion loss with a good extinction ratio within a wavelength

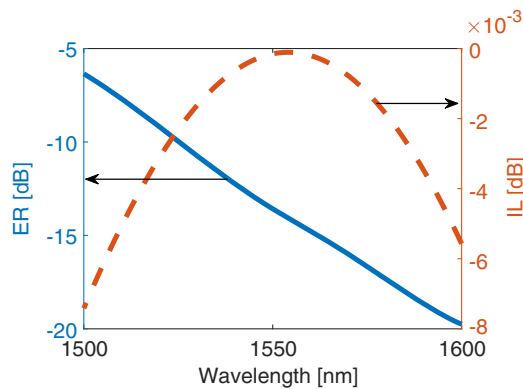


Fig. 11. Variation of the IL and ER with the wavelength (λ).

Table 1. Comparison Between the Proposed TE-Pass Polarizer and Those Reported in Literature

Year	Ref.	Device Length (μm)	ER (dB)	IL (dB)
2011	[8]	18	18.8	3.2
2011	[17]	3500	27	5
2012	[10]	30.0	23.0–28.0	2.0–3.0
2013	[9]	1.0	16.0	2.29
2015	[12]	1.35	18.0	0.004
2015	[18]	7	31.5	0.2
2016	[20]	8.3	18.2–21.2	0.16–0.36
2016	[11]	30	28	0.04
2016	[19]	7	20	0.13
2016	[13]	3.5	20.0	0.0635
2017	[14]	1.85	14.58	0.1639
–	This work	29	13.18	0.000108

range of 100 nm centered around 1550 nm. Table 1 shows a comparison between the proposed device performance and the ones provided in the literature. It is evident from this table that the proposed design has the lowest IL of -0.000108 dB with a good ER of -13.18 dB and compact device length of $29 \mu\text{m}$.

The suggested design has only two rings of air holes with elliptical core region. The cladding air holes with the same diameter are arranged in the widely used triangular lattice structure. Therefore, the fabrication process will not be difficult using the current PCF fabrication techniques [39]. In this context, PCF with air hole diameters of typically $0.1 \mu\text{m}$ or more can be fabricated using the fused array preform fabrication technique [40,41]. Further, the core region has an elliptical hole filled with silicon material that can be realized as reported in [42–44]. It is worth noting that three different triangular lattice PCFs have been fabricated by Belardi *et al.* [45] with ellipticity factors between 1.2 and 1.5. The ellipticity factor of the starting silica cane before the drawing process was equal to 1.9 [45]. Therefore, it is believed that PCF with proper ellipticity can be achieved by optimizing the drawing conditions (temperature, pressure, and speeds). Additionally, the suggested PCF design has elliptical core of major and minor radii of $0.3 \mu\text{m}$ and $0.11 \mu\text{m}$ in the same region of dimensions of the fabricated PCFs [45]. In order to selectively infiltrate the reported PCF with gold nanorods, the pressure filling technique can be used

[46]. Through the infiltration process, the Ti:Sa-laser-assisted polymer gluing can selectively open or inflate the air holes with diameter down to 500 nm . Next, the gold can be filled through the hollow channels at its melting point by using high pressure. A similar filling technique has been suggested to infiltrate the central hole only in [47] with similar dimensions to our proposed PCF. Furthermore, full flexibility in selective filling of PCFs [48] can be realized using a two-photon direct-laser writing technique. Therefore, it is believed that the suggested design can be experimentally fulfilled.

4. CONCLUSION

A TE-pass polarizer based on Si-core PCF with very low insertion losses has been proposed and characterized. At a device length of $29 \mu\text{m}$, a TE-pass polarizer has been achieved with a very low insertion loss of -0.000108 dB and a good extinction ratio of -13.18 dB. This device employs the low-loss and endless single-mode properties of PCF with the high birefringence associated with elliptical silicon core. Both FVEM and 3D-FDTD simulations show that the TM-core mode is cut off and attenuated rapidly along the propagation direction, unlike the TE-core mode that propagates with very low losses.

REFERENCES

- P. J. Winzer, "Modulation and multiplexing in optical communications," in *Conference on Lasers and Electro-Optics/International Quantum Electronics Conference* (Optical Society of America, 2009), p. CTuL3.
- P. J. Winzer and G. J. Foschini, "MIMO capacities and outage probabilities in spatially multiplexed optical transport systems," *Opt. Express* **19**, 16680–16696 (2011).
- J. A. H. Odoeze, O. M. Nawwar, and H. M. H. Shalaby, "J-rib waveguide as a mode-division demultiplexer," in *Proceedings of the Asia Communications and Photonics Conference (ACP)* (Wuhan, 2016), pp. AF1G.6(1–3).
- B. Stern, X. Zhu, C. P. Chen, L. D. Tzuan, J. Cardenas, K. Bergman, and M. Lipson, "On-chip mode-division multiplexing switch," *Optica* **2**, 530–535 (2015).
- S. Soudi and B. M. A. Rahman, "Design of a compact polarization splitter by using identical coupled silicon nanowires," *J. Lightwave Technol.* **34**, 4169–4178 (2016).
- D. Dai, Z. Wang, N. Julian, and J. E. Bowers, "Compact broadband polarizer based on shallowly-etched silicon-on-insulator ridge optical waveguides," in *Optical Fiber Communication Conference and Exposition and the National Fiber Optic Engineers Conference* (2011), pp. 1–3.
- D. Liang and J. E. Bowers, "Recent progress in lasers on silicon," *Nat. Photonics* **4**, 511–517 (2010).
- M. Alam, J. S. Aitchison, and M. Mojahedi, "Compact hybrid TM-pass polarizer for silicon-on-insulator platform," *Appl. Opt.* **50**, 2294–2298 (2011).
- Y. Huang, S. Zhu, H. Zhang, T.-Y. Liow, and G.-Q. Lo, "Cmos compatible horizontal nanoplasmonic slot waveguides TE-pass polarizer on silicon-on-insulator platform," *Opt. Express* **21**, 12790–12796 (2013).
- X. Sun, M. Z. Alam, S. J. Wagner, J. S. Aitchison, and M. Mojahedi, "Experimental demonstration of a hybrid plasmonic transverse electric pass polarizer for a silicon-on-insulator platform," *Opt. Lett.* **37**, 4814–4816 (2012).
- X. Sun, M. Mojahedi, and J. S. Aitchison, "Hybrid plasmonic waveguide-based ultra-low insertion loss transverse electric-pass polarizer," *Opt. Lett.* **41**, 4020–4023 (2016).
- S. I. Azzam and S. S. A. Obayya, "Ultra-compact resonant tunneling-based TE-pass and TM-pass polarizers for SOI platform," *Opt. Lett.* **40**, 1061–1064 (2015).

13. S. I. Azzam and S. S. A. Obayya, "Titanium nitride-based CMOS-compatible TE-pass and TM-pass plasmonic polarizers," *IEEE Photon. Technol. Lett.* **28**, 367–370 (2016).
14. M. F. O. Hameed, R. Zaghoul, S. I. Azzam, and S. S. A. Obayya, "Ultrashort hybrid plasmonic transverse electric pass polarizer for silicon-on-insulator platform," *Opt. Eng.* **56**, 017107 (2017).
15. A. H. Castro Neto, F. Guinea, N. M. R. Peres, K. S. Novoselov, and A. K. Geim, "The electronic properties of graphene," *Rev. Mod. Phys.* **81**, 109–162 (2009).
16. Q. Bao, H. Zhang, B. Wang, Z. Ni, C. Haley, Y. X. Lim, Y. Wang, D. Y. Tang, and K. P. Loh, "Graphene photonics and optoelectronics," *Nat. Photonics* **4**, 611–622 (2010).
17. Q. Bao, H. Zhang, B. Wang, Z. Ni, C. Haley, Y. X. Lim, Y. Wang, D. Y. Tang, and K. P. Loh, "Broadband graphene polarizer qiaoliang," *Nat. Photonics* **5**, 411–415 (2011).
18. X. Yin, T. Zhang, L. Chen, and X. Li, "Ultra-compact TE-pass polarizer with graphene multilayer embedded in a silicon slot waveguide," *Opt. Lett.* **40**, 1733–1736 (2015).
19. X. Yin, X. Ke, L. Chen, T. Zhang, J. Li, Z. Zhu, and X. Li, "Ultra-broadband TE-pass polarizer using a cascade of multiple few-layer graphene embedded silicon waveguides," *J. Lightwave Technol.* **34**, 3181–3187 (2016).
20. T. Zhang, X. Yin, L. Chen, and X. Li, "Ultra-compact polarization beam splitter utilizing a graphene-based asymmetrical directional coupler," *Opt. Lett.* **41**, 356–359 (2016).
21. S. Ghosh, D. Mandal, A. Chandra, and B. N. Shivakiran Bhaktha, "Graphene oxide integrated on-chip tunable waveguide polarizer," in *Frontiers in Optics* (Optical Society of America, 2017), p. FTu4A.3.
22. P. S. J. Russell, "Photonic-crystal fibers," *J. Lightwave Technol.* **24**, 4729–4749 (2006).
23. J. C. Knight, T. A. Birks, P. S. J. Russell, and D. Atkin, "All-silica signal-mode optical fiber with photonic crystal cladding," *Opt. Lett.* **21**, 1547–1549 (1996).
24. M. F. O. Hameed, A. M. Heikal, B. M. Younis, M. Abdelrazzak, and S. S. A. Obayya, "Ultra-high tunable liquid crystal-plasmonic photonic crystal fiber polarization filter," *Opt. Express* **23**, 7007–7020 (2015).
25. H. W. Lee, M. A. Schmidt, H. K. Tyagi, L. P. Sempere, and P. S. J. Russell, "Polarization-dependent coupling to plasmon modes on sub-micron gold wire in photonic crystal fiber," *Appl. Phys. Lett.* **93**, 10–13 (2008).
26. A. M. Heikal, F. F. K. Hussain, M. F. O. Hameed, and S. S. A. Obayya, "Efficient polarization filter design based on plasmonic photonic crystal fiber," *J. Lightwave Technol.* **33**, 2868–2875 (2015).
27. B. Li, M. Li, L. Peng, G. Zhou, Z. Hou, and C. Xia, "Research on dual-wavelength single polarizing filter based on photonic crystal fiber," *IEEE Photon. J.* **9**, 1–9 (2017).
28. W. Haensch, E. J. Nowak, R. H. Dennard, P. M. Solomon, A. Bryant, O. H. Dokumaci, A. Kumar, X. Wang, J. B. Johnson, and M. V. Fischetti, "Silicon CMOS devices beyond scaling," *IBM J. Res. Dev.* **50**, 339–361 (2006).
29. L. Lagonigro, N. Healy, J. R. Sparks, N. F. Baril, P. J. A. Sazio, J. V. Badding, and A. C. Peacock, "Low loss silicon fibers for photonics applications," *Appl. Phys. Lett.* **96**, 41105 (2010).
30. F. Yaman, H. Pang, X. Xie, P. LiKamWa, and G. Li, "Silicon photonic crystal fiber," in *Conference on Lasers and Electro-Optics/International Quantum Electronics Conference* (Optical Society of America, 2009), p. CTuDD7.
31. P. J. A. Sazio, A. Amezcua-Correa, J. R. H. C. E. Finlayson, T. J. Scheidemantel, N. F. Baril, B. R. Jackson, D. Won, F. Zhang, E. R. Margine, V. Gopalan, V. H. Crespi, and J. V. Badding, "Microstructured optical fibers as high-pressure microfluidic reactors," *Science* **311**, 1583–1586 (2006).
32. I. Kiyat, A. Aydinli, and N. Dagli, "A compact silicon-on-insulator polarization splitter," *IEEE Photon. Technol. Lett.* **17**, 100–102 (2005).
33. D. Dai and S. He, "Analysis of the birefringence of a silicon-on-insulator rib waveguide," *Appl. Opt.* **43**, 1156–1161 (2004).
34. COMSOL 5.1, "Multiphysics software," <https://www.comsol.com>.
35. Lumerical, "FDTD Solutions Software," <https://www.lumerical.com/tcad-products/fdtd/>.
36. G. P. Agrawal, *Nonlinear Fiber Optics*, 3rd ed. (Academic, 1989).
37. M. H. Lukas Chrostowski, *Silicon Photonics Design from Device to Systems* (Cambridge University, 2015).
38. W. Y. Crutchfield, H. Cheng, and L. Greengard, "Sensitivity analysis of photonic crystal fiber," *Opt. Express* **12**, 4220–4226 (2004).
39. C. A. G. Kalnins, H. Eberdorff-Heidepriem, N. A. Spooner, and T. M. Monro, "Radiation dosimetry using optically stimulated luminescence in fluoride phosphate optical fibres," *Opt. Mater. Express* **2**, 62–70 (2012).
40. P. Falkenstein, C. D. Merritt, and B. L. Justus, "Fused preforms for the fabrication of photonic crystal fibers," *Opt. Lett.* **29**, 1858–1860 (2004).
41. P. Falkenstein and B. L. Justus, "Fused array preform fabrication of holey optical fibers," U.S. patent 8,433,167 B2 (April 30, 2013).
42. Y. Yue, G. Kai, Z. Wang, T. Sun, L. Jin, Y. Lu, C. Zhang, J. Liu, Y. Li, Y. Liu, S. Yuan, and X. Dong, "Highly birefringent elliptical-hole photonic crystal fiber with squeezed hexagonal lattice," *Opt. Lett.* **32**, 469–471 (2007).
43. P. Szarniak, R. Buczynski, I. K. Dariusz Pysz, M. Franczyk, and R. Stepien, "Highly birefringent photonic crystal fibers with elliptical holes," *Proc. SPIE* **5950**, 59501L (2005).
44. N. A. Issa, M. A. van Eijkelenborg, M. Fellew, F. Cox, G. Henry, and M. C. J. Large, "Fabrication and study of microstructured optical fibers with elliptical holes," *Opt. Lett.* **29**, 1336–1338 (2004).
45. W. Belardi, G. Bouwmans, L. Provino, and M. Douay, "Form-induced birefringence in elliptical hollow photonic crystal 400 fiber with large mode area," *IEEE J. Quantum Electron.* **41**, 1558–1564 (2005).
46. H. W. Lee, "Plasmonic photonic crystal fiber," Ph.D. thesis (Max Planck Institute for Science of Light, 2012).
47. T. R. Wolinski, A. Czapla, S. Ertman, M. Tefelska, A. W. Domanski, E. Nowinowski-Kruszelnicki, and R. Dabrowski, "Tunable highly birefringent solid-core photonic liquid crystal fibers," *Opt. Quantum Electron.* **39**, 1021–1032 (2007).
48. M. Vieweg, T. Gissibl, S. Pricking, B. T. Kuhlmeier, D. C. Wu, B. J. Eggleton, and H. Giessen, "Ultrafast nonlinear optofluidics in selectively liquid-filled photonic crystal fibers," *Opt. Express* **18**, 25232–25240 (2010).